

Post maximum light and late time optical imaging polarimetry of type I superluminous supernova 2020znr

F. Poidevin^{1,2}, ^{*} C. M. B. Omand³, I. Pérez-Fournon^{1,2}, R. Clavero^{1,2}, R. Shirley^{4,5}, R. Marques-Chaves⁶, C. Jimenez Angel^{1,2}, S. Geier^{1,7}.

¹ Instituto de Astrofísica de Canarias, 38200 La Laguna, Tenerife, Canary Islands, Spain

² Departamento de Astrofísica, Universidad de La Laguna (ULL), 38206 La Laguna, Tenerife, Spain

³ The Oskar Klein Centre, Department of Astronomy, Stockholm University, AlbaNova, SE-10691 Stockholm, Sweden

⁴ Astronomy Centre, Department of Physics & Astronomy, University of Southampton, Southampton, SO17 1BJ, UK

⁵ Institute of Astronomy, University of Cambridge, Madingley Road, Cambridge, CB3 0HA, UK

⁶ Geneva Observatory, University of Geneva, Chemin Pegasi 51, CH-1290 Versoix, Switzerland

⁷ GRANTECAN: Cuesta de San José s/n, 38712 Breña Baja, La Palma, Spain

Accepted XXX. Received YYY; in original form ZZZ

ABSTRACT

Optical imaging polarimetry was conducted on the hydrogen poor superluminous supernova 2020znr during 3 phases after maximum light ($\approx +34$ days, $+288$ days and $+289$ days). After instrumental and interstellar polarization correction, all measurements are consistent with null-polarization detection. Modelling the light curve with a magnetar spin-down model shows that SN2020znr has similar magnetar and ejecta parameters to other SLSNe. A comparison of the best-fit values discussed in the literature on SN 2017egm and SN 2015bn, two hydrogen poor SLSNe showing an increase of polarization after maximum light, suggests that SN 2020znr has higher mass ejecta that may prevent access to the geometry of the inner ejecta with optical polarimetry. The combined information provided by spectroscopy and light curve analysis of type I SLSNe may be an interesting avenue to categorize the polarization properties of this class of transients. This approach would require to expand the sample of SLSNe polarimetry data currently available with early and late time epochs new measurements.

Key words: techniques: polarimetric – supernovae: general – supernovae: individual: 2020znr, 2015bn, 2017egm, 2018hti, LSQ14mo, PTF12dam.

1 INTRODUCTION

Superluminous supernovae (SLSNe) are core collapse supernovae showing explosions about 100 times brighter than common supernovae. While their population is quite rare (e.g. Schulze et al. 2021) based on current survey detection rates, and limited resources to classify all of them with spectroscopy (Nicholl 2021a), they have been subject of intense studies since their discovery about 15 years ago (Gal-Yam 2019a). This transient population is mainly subdivided in two classes, which are hydrogen-poor (SLSN-I) and hydrogen-rich (SLSN-II). Their light-curves show a disparity of shapes, and of rising and decreasing time scales, (Nicholl et al. 2017b; Lunnan et al. 2018b, 2020), likely subject to local and global environmental effects (Perley et al. 2016; Schulze et al. 2018, 2021), making their classification (Gomez et al. 2020; Sánchez-Sáez et al. 2021) and interpretation quite complex.

Several models were proposed to explain SLSNe. The three main models are the pair-instability model, the ejecta-circumstellar material interaction model, and the magnetar spin-down model (Moriya et al. 2018; Gal-Yam 2019a; Nicholl 2021b). Pair instability supernovae are the explosions of extremely massive ($\gtrsim 130 M_{\odot}$) stars

(Rakavy & Shaviv 1967; Barkat et al. 1967; Fraley 1968); the light curves of these explosion can be consistent with some slower SLSNe (Lunnan et al. 2016; Kozyreva et al. 2018; De Cia et al. 2018), but their spectra are predicted to be red and spectral models are inconsistent with observations in both the early and nebular phases (Dessart et al. 2012; Jerkstrand et al. 2016, 2017). Ejecta-CSM interaction, where the supernova ejecta collide with material previously ejected from the star, either through a binary interaction, stellar wind, or eruptive mass loss (Smith 2014) such as a pulsational pair instability (Woosley 2017), is usually used to explain SLSNe-II (Smith et al. 2010; Gal-Yam 2019a), but is also consistent with light curves for SLSNe-I (Tolstov et al. 2017; Ginzburg & Balberg 2012; Nicholl et al. 2014). The magnetar spin-down model, where the rotational energy of a newborn millisecond magnetar is used to power the supernova (Ostriker & Gunn 1971; Kasen & Bildsten 2010; Woosley 2010), can also fit most SLSN-I light curves (Nicholl et al. 2017b). Ejecta-CSM interaction and magnetar spin-down can be difficult to distinguish through photometry alone, but spectroscopic and multiwavelength follow-up have provided strong candidates for both magnetar powered supernovae (Milisavljevic et al. 2018; Eftekhari et al. 2019) and interaction powered supernovae (Lunnan et al. 2018a), although a hybrid model may be necessary to explain some SLSNe-I (Inserra et al. 2017; Yan et al. 2017).

* E-mail: fpoidevin@iac.es (IAC)

As for many other transients, SLSNe are intensively observed with spectroscopy. Analysis and modelling of time evolving spectral absorption features give access to the photosphere composition and dynamics (e.g. Gal-Yam 2019b). Analysis of large sample spectra database also provides information on possibly different channels leading to such explosions (e.g. Quimby et al. 2018; Könyves-Tóth & Vinkó 2021). Photometry also provides a wealth of information. The higher the sampling rate, the broader the wavelengths bandwidth coverage with multi-band photometry, the better the characterization of the time evolution of the luminosity via intense multicolor light curve modelling (e.g. Nicholl et al. 2017b; Guillochon et al. 2018; Kumar et al. 2021). It can be hard to distinguish various SLSN models using only optical emission, but both magnetar-driven supernovae and interaction-powered supernovae are expected to be bright in radio and X-rays at late times (Murase et al. 2015; Kashiyama et al. 2016; Omand et al. 2018), and various multiwavelength follow-up observations have been also carried out. Margutti et al. (2018) surveyed 26 SLSNe in X-rays at various post-explosion timescales, and only found emission from PTF12dam around its optical peak; X-rays were also detected previously in SCP06F6 (Levan et al. 2013), which was suggested to be due to an engine-powered ionization breakout (Metzger et al. 2014). Radio and millimetre observations have mostly found non-detections (Law et al. 2019; Murase et al. 2021; Eftekhari et al. 2021; Hatsukade et al. 2021a), but three sources have been detected: PTF10hgi (Eftekhari et al. 2019; Law et al. 2019; Mondal et al. 2020; Hatsukade et al. 2021b), which is consistent with the magnetar model; SN 2017ens (Coppejans et al. 2021a), which may be either due to a magnetar or CSM shock; and 2020tcw (Coppejans et al. 2021b), which was detected only months after explosion and is likely due to CSM interaction. An infrared excess in magnetar-driven supernova was predicted by Omand et al. (2019) due to heating of dust formed in the supernova, and which was observed recently in SN 2018bsz (Chen et al. 2021).

Optical polarimetry or spectropolarimetry has been investigated on a relatively small sample of SLSNe (Leloudas et al. 2015; Brown et al. 2016; Inserra et al. 2016; Leloudas et al. 2017; Cikota et al. 2018; Maund et al. 2019, 2020, 2021; Lee 2019, 2020; Cikota et al. 2018; Saito et al. 2020). Most of the observations were obtained close to peak maximum light, and no significant polarization detection was found ($< 3\sigma$). Up to date, the most stringent detections have been obtained on only two different transients. Inserra et al. (2016) and Leloudas et al. (2017) discuss null-polarization detection on 2015bn during 4 phases before maximum light but an increase up to about 1.5 % during later phases (from +5.4 up to +45.8 days). Similarly, Maund et al. (2019) show null-polarization detection during early phases on 2017egm given that the possible polarization signal, of order 1% detected at less than 2σ with imaging techniques, was attributed to the spiral arm in the proximity to the position of 2017egm. On the other hand, using spectropolarimetry observations, Saito et al. (2020) were able to show that the degree of polarization associated to 2017egm significantly changes from that measured at the earlier phase with an intrinsic polarization of ~ 0.2 % during early phases and an intrinsic polarization ~ 0.8 % in the late phase (+185 days).

In this work we present the first result, from a ten hour linear polarimetry survey, designed to explore the frequency of objects such as SN 2015bn and SN 2017egm. These results were obtained on the H-poor SN 2020znr during mainly 2 distinct epochs. This transient is located at (RA, Dec) = (109.776773°, 23.885371°), J2000. It was discovered by Nordin et al. (2020) on November 12, 2020

from ZTF¹ public alerts (Bellm et al. 2019). The discovery magnitude obtained with the ZTF-cam mounted on the Palomar 1.2 meter Oschin was of 19.77 mag in the g-filter (AB system). The transient was later classified as a SLSN-I at a redshift $z=0.1$ by Ihanec et al. (2020) from the analysis of a spectrum obtained by the extended Public ESO Spectroscopic Survey of Transient Objects (ePESSTO; Smartt et al. 2017) collaboration. The spectrum is publicly available on the Transient Name Server² (TNS). The transient is very likely associated to the low brightness feature observed in the Dark Energy Camera Legacy Survey (DECaLS)³, Data Release 9 (DR9) at position (RA, Dec) = (109.7767°, 23.8854°), J2000, of apparent magnitudes $g=23.96$, $r=23.64$, $z=23.50$ mag, i.e. of absolute magnitudes -14.32, -14.64 and -14.78 mag, respectively, assuming it is at the same redshift as the SLSN at $z=0.1$.

2 OBSERVATIONS

2.1 Spectroscopy

The ePESSTO+ collaboration spectrum of SN 2020znr was obtained with the ESO-NTT / EFOSC2 on November 17, 2020. We also obtained a spectrum about 122 days later, on March 19, 2021. This second epoch spectrum was obtained with the Liverpool Telescope (LT) SPectrograph for the Rapid Acquisition of Transients (SPRAT) (Steele et al. 2004; Piascik et al. 2014) with a total integration time of 3×200 seconds through $1.8''$ with the blue-optimized grating configuration starting at UTC time = 21 : 38 : 45.147. The two spectra are shown in Figure 1. Also shown in the Figure are the transmission of the V- and R-band filters mounted on the Alhambra Faint Object Spectrograph and Camera (ALFOSC) used to get linear polarimetry data discussed in the next section.

The two spectra are compared to other spectra obtained on SLSN-I. The first epoch spectrum is similar to early epochs spectra showing a blue continuum with absorption features that have been identified as O_{II} by Quimby et al. (2011). Such features have been further discussed and modeled by Gal-Yam (2019b). The simple method proposed by Gal-Yam (2019b) shows that early phase SLSNe spectra are mainly probing the photosphere which can be mostly described by absorptions from single transitions with a single photospheric velocity. An early phase, 21 days before maximum light, spectrum of PTF12dam is shown in Figure 1 for comparison. This spectrum was the best match solution from a fitting template analysis with SNID, the SuperNova IDentification code,⁴ (Blondin & Tonry 2007) using the Quimby et al. (2018) spectra database ingested in our custom SNID template library. Later epochs spectra from PTF12dam obtained after maximum light that resemble SN Ic (Pastorello et al. 2010) spectra are also found to be relatively good candidates for comparisons with the LT SPRAT spectrum. From the SNID analysis the best phase estimate of the LT SPRAT spectrum is +100 days.

2.2 Photometry

The ZTF g- and r-band public photometry data obtained on SN 2020znr (ZTF object ZTF20acphdgcg, Pan-STARRS 1 object PS20lkc, ATLAS object ATLAS20bgae, Gaia object Gaia20fkx)

¹ Zwicky Transient Facility, <https://www.ztf.caltech.edu>.

² Transient Name Server, <https://www.wis-tns.org/2020znr>

³ Legacy Survey, <https://www.legacysurvey.org/>

⁴ <https://people.lam.fr/blondin.stephane/software/snid/>

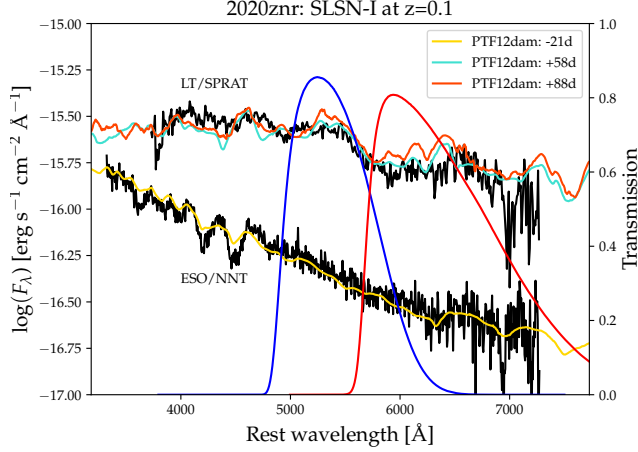


Figure 1. Spectra obtained on SN 2020znr. Plots of spectra of PTF12dam obtained at various phases are also displayed for comparison. The transmission curves of the V- and R-band filters mounted on the ALFOOSC are shown with the blue and red curves, respectively.

were retrieved from the Lasair broker⁵ (Smith et al. 2019). The ATLAS forced photometry data obtained on ATLAS object ATLAS20bgae were retrieved from the ATLAS public server⁶ (Tonry et al. 2018). They were clipped and binned to one day using the publicly available code `plot_atlas_fp.py`⁷. The public ZTF data and the public stacked and binned ATLAS data are displayed in Figure 2. They were obtained at Modified Julian Date (MJD) ranging in $\text{MJD} = [59145.6 - 59532.5]$ days. Maximum light occurred close to $\text{MJD} \approx 59227$ days as estimated from the g-band light curve. This means that polarimetry was obtained at phases $\approx +34$, $\approx +238$ and $\approx +239$ days, while spectroscopy would have been obtained at phases ≈ -57 and $\approx +66$ days. Also shown in the Figure is the linear polarization degree obtained at one epoch in the V- and R-filters and at two close epochs in the R-filter. These results will be discussed further. A compilation of the photometry used in this work is given in the tables displayed in section B.

2.3 Polarimetry

The observations log of the imaging polarimetry obtained with ALFOOSC on the Nordic Optical Telescope (NOT) is displayed in Table 1. Linear polarimetry is made using a half wave plate in the FAPOL unit and a calcite plate mounted in the aperture wheel. The calcite plate provides the simultaneous measurement of the ordinary and the extraordinary components of two orthogonal polarized beams (see Figure 3). The half wave plate can be rotated in steps of 22.5° from 0° to 337.5° . As a standard, 4 angles are used (0° , 22.5° , 45° , and 67.5°), which we used during our observations as referred to with the factor 4 used in the exposure time calculations displayed in Table 1.

The reduction of the polarimetry data was done using our own

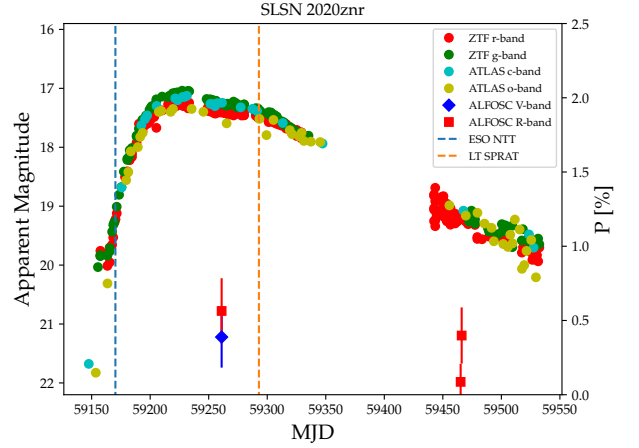


Figure 2. ZTF g- and r-band, and ATLAS c- and o-band light curve of SN 2020znr. The epochs when spectroscopy was obtained are shown with dashed-lines. The linear polarization degree, P , obtained at 3 epochs is also shown by the diamond and square symbols. The scale is given on the right-axis.

Table 1. Observations log of the imaging polarimetry observations.

UT Time	Object	Exp. Time [s]	Filter	Seeing ["]
2021-02-16 01:07	BD+52913	4×3	V	1.7
2021-02-16 01:08	BD+52913	4×3	R	1.7
2021-02-16 01:11	HD251204	4×3	V	1.3
2021-02-16 01:12	HD251204	4×3	R	1.3
2021-02-16 01:14	2020znr	$3 \times (4 \times 60)$	V	1.2
2021-02-16 01:24	2020znr	$3 \times (4 \times 60)$	R	1.0
2021-09-09 04:40	BD+52913	$4 \times (4 \times 10)$	R	0.4
2021-09-09 04:47	HD251204	$6 \times (4 \times 2)$	R	0.6
2021-09-09 05:02	2020znr	$4 \times (4 \times 180)$	R	0.4
2021-09-10 05:29	BD+52913	$2 \times (4 \times 10)$	R	0.6
2021-09-10 05:34	HD251204	$3 \times (4 \times 2)$	R	0.6
2021-09-10 05:02	2020znr	$2 \times (4 \times 180)$	R	0.6

pipeline. Flat and bias frames obtained during the nights of the observations were cropped at the size of the observation frames. The observation frames were then bias subtracted and flat-fielded using median frames of the bias and flat images, respectively. The zero level of each reduced observation frame was assessed using the python package PHOTUTILS then DAOfind was used to produce a list of the sources detected above a given threshold in each final frame. Circular aperture photometry was then operated on each detected source taking into account the average seeing information. Aperture photometry is preferred over PSF fitting because the polarized images are not circular after the half wave plate. These apertures cover up to about 2 to 3 times the full width at half maximum (FWHM). At this stage a total flux in Analog-to-Digital Units (ADU) was obtained on each ordinary and extraordinary images of the astrophysical sources of interest.

Raw Stokes Q and U parameters were calculated using the formalism provided by Magalhaes et al. (1984) and Ramírez et al. (2017). From each reduced frame obtained at a half waveplate angle posi-

⁵ <https://lasair.roe.ac.uk/object/ZTF20acphdgcg/>

⁶ <https://fallingstar-data.com/forcedphot/>

⁷ <https://gist.github.com/thespacedoctor/86777fa5a9567b7939e8d84fd8cf6a76>.

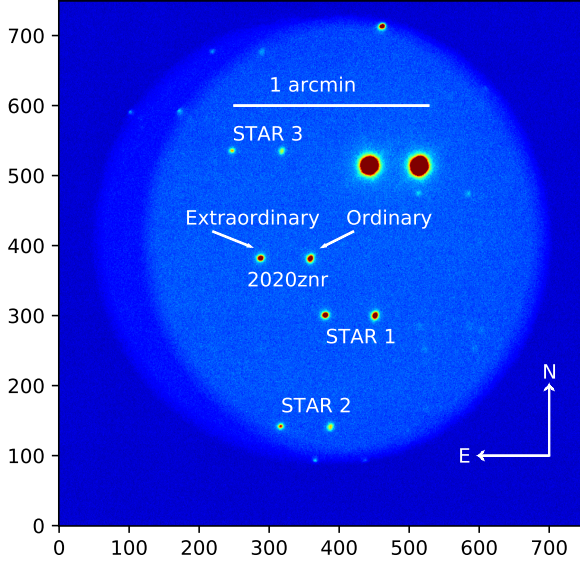


Figure 3. Linear polarimetry of SN 2020znr with ALFOSC in one of the V-band flat-field and bias corrected raw data frame (file ALEb150089.fits) obtained with the half-wave plate at a position angle of 0.0° . Each pixel embeds the number of counts obtained after an exposure of 60 seconds. Imaging polarimetry was acquired through half-wave plates positions angles at 0.0° , 22.5° , 45.0° and 67.5° . The calcite plate splits the light from the several objects into Ordinary images and Extraordinary images separated by about $15''$ from each other.

tion, i , we first calculate the ordinary and extraordinary fluxes, $F_{o,i}$ and $F_{e,i}$, respectively. The modulation of the intensity with the half waveplate position, z_i , is given by the expression:

$$z_i = \frac{F_{e,i} - F_{o,i}(F_e^T/F_o^T)}{F_{e,i} + F_{o,i}(F_e^T/F_o^T)} = Q \cos(4\psi_i) + U \sin(4\psi_i), \quad (1)$$

where, F_o^T , and F_e^T , are the total ordinary and extraordinary fluxes, respectively, summed over the waveplate positions and, ψ_i , is the half-wave plate position angle at position, i . Following the prescription given by Magalhaes et al. (1984) the solution for the Stokes parameters Q and U are:

$$Q = \frac{2}{\mu} \sum_i z_i \cos(4\psi_i), \quad (2)$$

$$U = \frac{2}{\mu} \sum_i z_i \sin(4\psi_i), \quad (3)$$

where, μ , is the total number of half-wave plate positions. Once the Stokes parameters are calculated, one can directly obtain the fraction of polarization:

$$P = \sqrt{Q^2 + U^2}, \quad (4)$$

and the polarization angle position:

$$\theta = \frac{1}{2} \tan^{-1} \frac{U}{Q}, \quad (5)$$

where θ is counted positively from north to east in the equatorial reference frame after correction of the zero-angle calibrated with a

polarized standard star. Assuming the uncertainties on Stokes parameters, Q , and, U , are of the same order and therefore that $\sigma_Q = \sigma_U = \sigma_P$, we follow Magalhaes et al. (1984) and Naghizadeh-Khouei & Clarke (1993) and calculate the errors as:

$$\sigma_P = \frac{1}{\sqrt{\mu-2}} \sqrt{\frac{2}{\mu} \sum_i z_i^2 - Q^2 - U^2}, \quad (6)$$

$$\sigma_\theta = 28^\circ \cdot 65 \frac{\sigma_P}{P}. \quad (7)$$

In the following we will discuss the fraction of polarization obtained without applying any debiasing method. A test of our polarization data reduction method is given in section A where the output of our pipeline is compared to the results obtained by Lee (2020) on SN 2020ank ALFOSC polarimetry data. Field stars, STAR 1, STAR 2 and STAR 3, displayed in Figure 3 are field stars that will be considered to make estimates of the Milky Way Interstellar Polarization (ISP).

3 ANALYSIS

3.1 Light Curve Modelling

We fit the multi-band light curve using the magnetar spin-down model in the Modular Open-Source Fitter for Transients (MOSFiT) code, which uses a Markov Chain Monte Carlo (MCMC) algorithm to perform Bayesian parameter estimation for supernova light curves (Guillochon et al. 2018). We use the Dynesty sampler (Speagle 2020; Higson et al. 2019), which utilizes dynamic nested sampling. The uncertainty presented is only the statistical uncertainty in the fits, and does not include systematic uncertainty inherent in the simplified one-zone MOSFiT model.

The magnetar-model fits are shown in Figure 4 and the most physically relevant parameters are listed in Table 2, with their posteriors shown in Figure 5. The model provides a good fit to the data, although it does overestimate luminosity during the pre-peak rise. The physical parameters we find are $B_\perp \approx 5 \times 10^{13}$ G, $M_{\text{NS}} \approx 1.7 M_\odot$, $P_{\text{spin}} \approx 3.0$ ms, $M_{\text{ej}} \approx 21 M_\odot$, and $v_{\text{ej}} \approx 5500$ km/s, where B_\perp is the magnetar magnetic field strength, M_{NS} is the neutron star mass, P_{spin} , is magnetar spin period, M_{ej} is the ejecta mass and, v_{ej} is the ejecta velocity. These best fit parameters and uncertainties are the median and 1σ values from the one-dimensional posterior for each of the parameters. While the median value is close to the most-likely value for M_{ej} and v_{ej} , which have symmetric posteriors, the median value is lower than the most-likely value by $\sim 1\sigma$ for B_\perp , M_{NS} , and P_{spin} , which are asymmetric around the median value (this is also seen in the joint posterior for all SLSNe examined by Nicholl et al. (2017b)) and feature a steady increase in probability as the parameters increase, followed by a sharp cutoff. This cutoff is likely due to M_{NS} reaching the maximum of its prior. These parameters are fairly typical of SLSNe-I (Nicholl et al. 2017b; Villar et al. 2018; Blanchard et al. 2020; Yin et al. 2021), except for the ejecta mass, which is larger than average, although not abnormally so, as will be discussed further in Section 4. However, SN 2020znr has a broad light curve and fades slowly, which is indicative of a large ejecta mass. The total kinetic energy of the ejecta is calculated to be $E_K \approx 4 \times 10^{51}$ ergs. The mass of the progenitor star, $M_* = M_{\text{NS}} + M_{\text{ej}} \approx 23 M_\odot$, which is consistent with the 3.6-40 M_\odot range inferred in the mass distribution found by Blanchard et al. (2020).

We find strong correlations between B_\perp , M_{NS} , and P_{spin} in the 2D posterior distributions of these parameters (see Figure 5). These

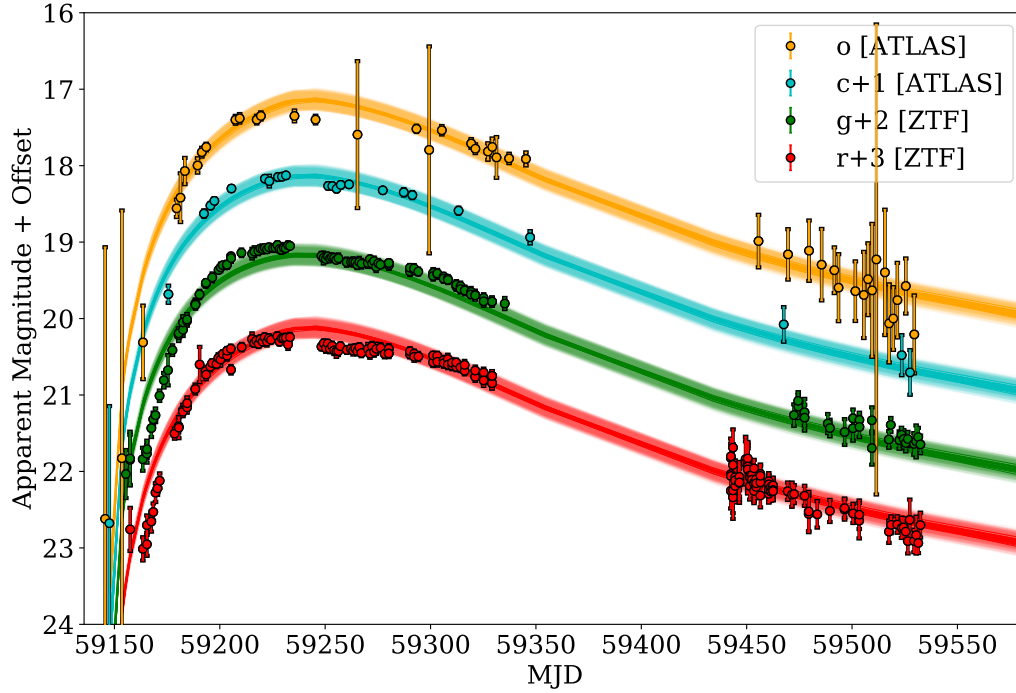


Figure 4. Multi-band light curve of SN 2020znr inferred from the magnetar-model, with each band offset for clarity. The filled area shows the range of most likely models generated by MOSFiT. See Section 3.1 for details.

Table 2. Median and 1σ best fit parameters for magnetar models. Parameters obtained on SN 2020znr are discussed in Section 3.1 and compared to those obtained on SN 2015bn and SN 2017egm in Section 4.

Parameter Symbol	Definition	Prior 2020znr This work	Best Fit Value 2020znr This work	Best Fit Value 2015bn Nicholl et al. (2017b)	Best Fit Values 2017egm Nicholl et al. (2017a)	Units
B_{\perp}	Magnetar Magnetic Field Strength	[0.1,10]	$0.51^{+0.10}_{-0.13}$	$0.31^{+0.07}_{-0.05}$	[0.7 – 1.7]	10^{14} G
M_{NS}	Neutron Star Mass	[1.0,2.0]	$1.68^{+0.21}_{-0.31}$	$1.78^{+0.28}_{-0.23}$...	M_{\odot}
P_{spin}	Magnetar Spin Period	[1,10]	$2.80^{+0.26}_{-0.39}$	$2.16^{+0.29}_{-0.17}$	[4–6]	ms
$\log(M_{\text{ej}})$	Ejecta Mass	[-1,2]	$1.33^{+0.03}_{-0.03}$	$1.09^{+0.08}_{-0.13}$	[0.3–0.6]	M_{\odot}
v_{ej}	Ejecta Velocity	[1,20]	$5.56^{+0.13}_{-0.13}$	$5.46^{+0.16}_{-0.14}$...	10^3 km/s

correlations have been observed in the posteriors of magnetar model fits of some supernovae (e.g., SN2015bn; Nicholl et al. 2017b), but are not seen in others (e.g., SN2018lfe; Yin et al. 2021). It is unknown why only some SLSNe show these correlations, and while this bimodality could have a physical origin, it is likely due some supernovae being more well sampled and having stronger constraints on system parameters.

3.2 Polarimetry null-detection

Using the formalism described in section 2.3 we first calculated the average raw Stokes parameters, $\overline{Q}^{(a)}$, and $\overline{U}^{(a)}$, obtained with Bessel -V or -R filters on the polarized and unpolarized stars, on the three field stars identified in Figure 3, and on the main target SN 2020znr. Their values are displayed in columns 4 and 5 in Table 3. The Instrumental Polarization (*IP*) of the ALFOSC imaging polarimeter

estimated with the unpolarized star, BD+52913, shows Stokes *Q* and *U* of order 0.1% or below (see columns 6 in Table 3). These values were subtracted from the raw Stokes parameter estimates on all other targets. The calibration of the Zero Polarization Angle (*ZPA*) of the experiment was carried out using the polarized star HD251204 (see columns 7 and 8 in Table 3). Assuming HD251204 has a polarization angle of 147° (Turnshek et al. 1990) in both V- and R-bands we got *ZPA*, estimates of 83.9° and 87.7° , respectively. These values are subsequently used to correct for the *IP* corrected Stokes *Q* and *U* of the remaining sources of interest (STAR 1, 2 and 3) as shown in columns 9 and 10 in Table 3.

To obtain the level of linear polarization of SN 2020znr, the remaining step is to assess the level of polarization produced by the interstellar medium in our galaxy. To do so we first cross-matched the coordinates of field stars 1, 2 and 3 with the GAIA Early Data Release 3 (EDR3) distances catalog (Bailer-Jones et al. 2021). The median of the geometric distance posterior, *rg_{eo}*, and the median of

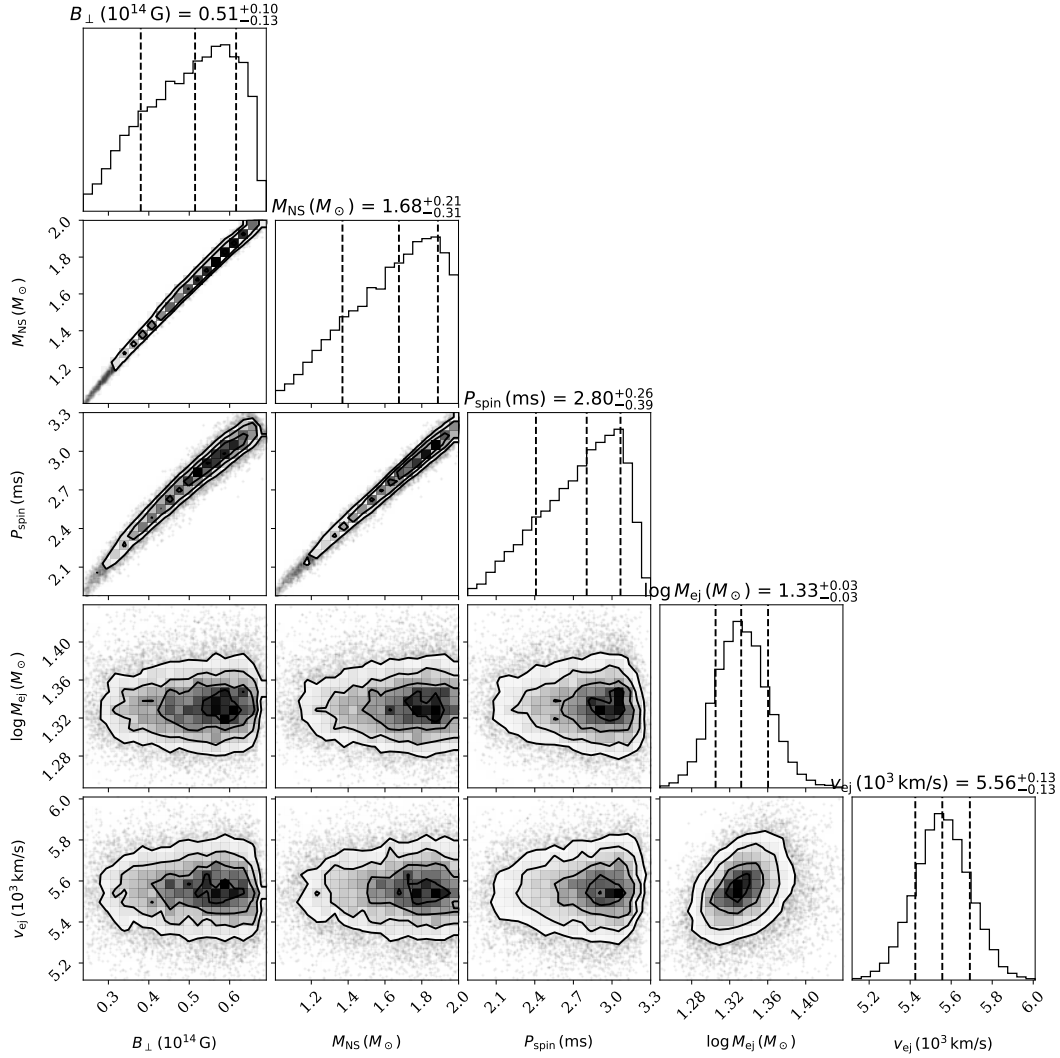


Figure 5. 1D and 2D posterior distributions of the magnetar model parameters. Median and 1σ values are marked and labeled - these are used as the best fit values (discussed in text).

the photogeometric distance posterior, rp_{geo} , ranging from about 2000 pc to about 4000 pc are displayed in Table 4. In addition to fields stars 1, 2 and 3 observed with ALFOSC we also searched for candidates in the Heiles (2000) agglomeration file catalog. This catalog is a compilation of linear polarization measurements, mainly in the V-band, on relatively bright Galactic stars. Our main selection criterion was the angular distance to SN 2020znr as shown in the last column of Table 5. The closest star is HD 56986, at an angular distance 0.70° , which we rejected from the Table since it is a spectroscopic binary. All the other stars are at an angular distance lower than 2° from SN 2020znr at heliocentric distance between 50 pc and 800 pc. They have very low polarization degrees consistent with null-polarization within the uncertainties. Since all the detections are less than 1σ detections, are at heliocentric distances lower than 1000 pc and more importantly lie at angular distances higher than 1° from SN 2020znr, we followed the recommendation given by Tran (1995) and didn't include them for estimating the Milky Way ISP. STAR 2 is at the higher heliocentric distance and it is therefore our best candidate for estimating our Galaxy ISP contribution. Hence, we first made estimates of SN 2020znr intrinsic polarization degree

by subtracting its *IP* and *ZPA* corrected Stokes parameters from the *IP* and *ZPA* corrected Stokes parameters obtained on SN 2020znr. Since one can expect variations from one line-of-sight to the other, as a second step, the *IP* and *ZPA* corrected Stokes parameters obtained on field stars STAR 1, STAR 2 and STAR 3 were weighted averaged by using the uncertainties to determine the weights, to get a statistical estimate of the Milky Way ISP along line-of-sights probing column densities up to about 2000 pc to 4000 pc, and subtracted from the *IP* and *ZPA* corrected Stokes parameters obtained on SN 2020znr.

The final levels of polarization obtained on SN 2020znr are displayed in the last column of Table 3 and both methods lead to similar conclusions: all the results are consistent with a null level of polarization within the uncertainties (i.e. all polarization signal-to-noise ratio are $< 3\sigma$). However, the variation of these constraints on the final level of polarization reflects the various total integration times defined in our observing strategy displayed in Table 3. Another important factor is the seeing, which changed from one night to the other. From these two points of view, the first observations obtained in the R- and V-bands on February 2021 were done when SN 2020znr apparent magnitudes were of order 17.5 in the ZTF r-band (see Fig-

Table 3. Polarimetry results. ^(a): Stokes parameters, \overline{Q} and \overline{U} , directly obtained from the ALFOSC data frames Extraordinary and Ordinary images without applying any further corrections. ^(b): instrumental polarization estimates. ^(c): instrumental polarization corrected. Assuming HD251204 has a polarization angle of 147° in V- and R-bands the zero polarization angle, ZPA , estimates are 83.9° and 87.7° , respectively. ^(d): IP and ZPA corrected. ^(e): IP and ZPA corrected + Milky Way Interstellar Polarization corrected with Stokes parameters obtained on star 2^(f) (see values shown in bold and underlined, and see text for details), which is at the largest heliocentric distance, then with weighted average Stokes parameters obtained on stars STAR 1, STAR 2 and STAR 3^(g) (See values only shown in bold and see text for details).

Date	Source	filter	$\overline{Q}^{(a)}$	$\overline{U}^{(a)}$	$P[\%]^{(b)}$	$P[\%]^{(c)}$	$\theta[^\circ]^{(c)}$	$P[\%]^{(d)}$	$\theta[^\circ]^{(d)}$	$P[\%]^{(e)}$
2021-02-16	BD+52913	V	-0.08	0.07	0.11 ± 0.07
...	HD251204	V	-2.91	3.93	...	4.78 ± 0.13	63.13 ± 0.75
...	STAR 1	V	-0.35	0.22	0.31 ± 0.17	159.23 ± 15.56	...
...	STAR 2	V	0.14	0.33	0.34 ± 0.28	108.06 ± 24.11	...
...	STAR 3	V	0.53	-0.00	0.62 ± 0.22	80.42 ± 10.35	...
...	ISP	V	0.00	0.00	0.06 ± 0.13	102.38 ± 66.00	...
...	2020znr ^(f)	V	-0.42	-0.25	0.81 ± 0.34
...	2020znr ^(g)	V	-0.42	-0.25	0.44 ± 0.21
2021-02-16	BD+52913	R	-0.06	-0.10	0.12 ± 0.16
...	HD251204	R	-2.49	4.29	...	5.01 ± 0.24	59.50 ± 1.37
...	STAR 1	R	-0.29	-0.04	0.23 ± 0.19	169.75 ± 24.07	...
...	STAR 2	R	-0.09	-0.23	0.14 ± 0.22	36.47 ± 44.48	...
...	STAR 3	R	-0.41	0.21	0.46 ± 0.32	156.43 ± 19.75	...
...	ISP	R	0.00	0.00	0.06 ± 0.14	169.67 ± 65.05	...
...	2020znr ^(f)	R	-0.51	-0.17	0.43 ± 0.32
...	2020znr ^(g)	R	-0.51	-0.17	0.59 ± 0.22
2021-09-08	BD+52913	R	-0.05	0.00	0.05 ± 0.03
...	HD251204	R	-2.51	4.18	...	4.85 ± 0.04	60.26 ± 0.26
...	STAR 1	R	-0.25	0.08	0.21 ± 0.07	166.57 ± 9.61	...
...	STAR 2	R	-0.09	-0.00	0.04 ± 0.11	0.03 ± 73.54	...
...	STAR 3	R	-0.24	-0.08	0.20 ± 0.11	7.91 ± 16.17	...
...	ISP	R	0.00	0.00	0.05 ± 0.06	174.86 ± 32.60	...
...	2020znr ^(f)	R	0.12	-0.06	0.22 ± 0.14
...	2020znr ^(g)	R	0.12	-0.06	0.09 ± 0.11
2021-09-09	BD+52913	R	-0.05	0.13	0.14 ± 0.07
...	HD251204	R	-2.48	4.24	...	4.78 ± 0.08	60.31 ± 0.48
...	STAR 1	R	-0.22	-0.02	0.23 ± 0.13	16.63 ± 16.51	...
...	STAR 2	R	-0.42	-0.30	0.56 ± 0.09	21.15 ± 4.64	...
...	STAR 3	R	-0.11	-0.12	0.26 ± 0.13	34.36 ± 14.56	...
...	ISP	R	0.00	0.00	0.12 ± 0.07	22.94 ± 16.04	...
...	2020znr ^(f)	R	-0.05	-0.29	0.37 ± 0.20
...	2020znr ^(g)	R	-0.05	-0.29	0.40 ± 0.18

Table 4. Gaia EDR3 distances to the field stars, STAR 1, STAR 2 and STAR 3, displayed in Figure 3. Parameter, r_{geo} , is the geometric distance, while parameter, r_{pgeo} , is the photogeometric distance (see [Bailer-Jones et al. 2021](#), for details)

Star name	RA (J2000) [$^\circ$]	Dec (J2000) [$^\circ$]	r_{geo} [pc]	r_{pgeo} [pc]
STAR 1	109.7707	23.8805	2018.19177	1997.0564
STAR 2	109.7749	23.8710	4084.69873	3371.26392
STAR 3	109.7707	23.8945	2114.16211	2391.48169

ure 2). At that time we used relatively short integration times on the unpolarized standard star, BD+52913, and the total integration time on SLSN 2020znr and the 3 fields stars was of 12 minutes. The DESI Legacy Survey DR9 apparent magnitudes of STAR 1, STAR 2 and STAR 3 displayed in Figure 3 are 17.41, 18.43, 18.95 in the g-band, and 16.84, 17.86, 18.12 in the r-band, respectively, i.e. at about the same level or less bright than SN 2020znr at that time. Propagating the instrumental polarization (IP) or order 0.1% on the Q , and U , Stokes parameters of order 0.3% to 0.6% obtained on each of these stars lead to relatively high estimates of the polarization level, but

once combined together, the measurements give a weighted average level ISP of $0.06 \pm 0.13\%$, in both bands. A result which is in line with the very low level of polarization obtained from starlight polarization on brighter stars in the vicinity of SN 2020znr on a square area of size 5° centred on its coordinates (see Table 5). Using only STAR 2 the Milky Way ISP contribution is found to be slightly higher, of $0.34 \pm 0.28\%$ in V-band, and of $0.14 \pm 0.22\%$ in R-band.

More than 6 months after the first polarimetry measurement, when SN 2020znr was 1.5 magnitudes fainter, we expected to detect a larger polarization degree than the one measured during the first polarimetry epoch. In order to reach a polarization signal-to-noise ratio at least $> 3\sigma$, we used a total integration time $4 \times$ higher in the R-band only (see log for the first night of September 2021, in Table 1), under two times better seeing conditions. These two factors combined together lead to a total weighted average $ISP = 0.05 \pm 0.06\%$, i.e. of the same order as on the field stars displayed in Table 5, all about or more than 8 magnitudes brighter than STAR 1, STAR 2 and STAR 3 and at heliocentric distances lower than 1000 pc. A level of precision also reached with STAR 2 whose ISP level is $ISP = 0.04 \pm 0.11\%$. These two ISP estimates lead to a stringent constraint on the intrinsic level of polarization obtained on SN 2020znr of about $0.1 \pm 0.1\%$ using STAR 1, STAR 2 and STAR 3, and of about $0.22 \pm$

0.14%, using STAR 2 only, i.e. fully consistent with 0%. In order to double check this result, the observations repeated on the following night under similar seeing conditions but with two times shorter integration times lead to a level of polarization of about $0.4 \pm 0.2\%$, still consistent with 0%. A visual summary of all these results can be seen on the $Q - U$ plots displayed in Figure 6 for each polarimetry epoch.

We point out that the object observed in the Legacy survey of magnitude $g = 23.96$ (see introduction section), very likely the host of SN 2020znr, is very faint with respect to the brightness of SN 2020znr. An intrinsic polarization degree associated to this feature, very likely a blue dwarf galaxy of absolute magnitudes, -14.32 mag in g-band, and -14.64 mag in r-band, assuming a redshift $z = 0.1$, is therefore not expected to contribute to the total polarization degree measured on SN 2020znr. On the other hand, the light emitted by SN 2020znr could be polarized by aligned dust grains pervading such a dwarf galaxy, even though it is a low metallicity galaxy. Dust polarization properties of such galaxies are not known and one can not discard the existence of magnetically aligned dust grains in such environments. For comparison, the low metallicity Magellanic clouds of absolute magnitude of about -18 mag in V-band, are pervaded by complex magnetic fields aligning dust grains at the origin of starlight polarization (e.g. Lobo Gomes et al. 2015). Our time-dependent observations can not directly help distinguish an intrinsically null polarization signal from an intrinsic polarization signal from SN 2020znr that is partly cancelled by its host ISP. On one hand, however, if the host ISP is not null it is expected to be uniform with time. On the other hand, comparisons with previous studies (see section 1 and section 4) strongly suggests that the intrinsic polarization of SLSNe are almost null during early phases (see the Introduction section). If SN 2020znr falls into such a category, therefore, one could assume that the ISP from its host is negligible in our detections. This is the hypothesis that will sustain our discussion in the following section.

4 DISCUSSION

Contrary to what has been observed on SN 2015bn a few days after maximum light, and on SN 2017egm about +185 days after maximum light, polarimetry on SN 2020znr does not show an increase of the degree of polarization, departing from null-polarization, at late time epochs ($\approx +238$ and $+239$ days). In the following we discuss further comparisons between SN 2020znr, SN 2015bn, and SN 2017egm, that may help to better understand this difference.

Figure 7 shows the absolute magnitude light curves of SN 2020znr, SN 2015bn, and SN 2017egm. The distance modulus was calculated using the *Planck* 2018 Flat Λ -CDM cosmology model ($\Omega_0 = 0.31$, $H_0 = 67.7$ km/s) (Planck Collaboration et al. 2020). For SN 2020znr we use a redshift $z = 0.1$ while for SN 2015bn and SN 2017egm we use redshifts $z = 0.1136$ and $z = 0.030721$, respectively. Photometry on SN 2015bn and SN 2017egm was retrieved from the OSC⁸ (Guillochon et al. 2017). Light curves comparisons show smaller fading timescales for SN 2017egm and SN 2015bn than for SN 2020znr, as well as a shorter rising timescale for SN 2017egm while SN 2020znr and SN 2015bn show similar rising timescales. At maximum light SN 2015bn appears to be more luminous (≈ -22 mag) than SN 2017egm (≈ -21.6 magnitudes) and SN 2020znr (≈ -21.2 magnitudes). Magnetar models of SN 2015bn and SN 2017egm light curves have been explored and discussed by

Nicholl et al. (2017b) and Nicholl et al. (2017a), respectively. Some of the parameters obtained from these analyses are displayed in Table 2 for comparison with the best fit value parameters obtained on SN 2020znr. They show that SN 2017egm, the fastest transient of the three sources, has an estimated ejected mass, M_{ej} , of order $2-4 M_{\odot}$, while for SN 2015bn and SN 2020znr M_{ej} is of $\approx 12 M_{\odot}$ and $\approx 21 M_{\odot}$, respectively. SN 2015bn and SN 2020znr have ejecta velocity of ≈ 5500 km/s each, and total kinetic energy of the same order, with $E_K \approx 4 \times 10^{51}$ ergs for SN 2020znr, and $E_{min,K} \approx 3.45 \times 10^{51}$ ergs for SN 2015bn (Nicholl et al. 2017b), while SN 2017egm has a total kinetic energy of $\approx 1 - 2 \times 10^{51}$ ergs and an ejecta velocity of ≈ 5500 km/s. All put together, these differences could explain why SN 2017egm is such a quick transient with respect to SN 2015bn and SN 2020znr. In addition, with similar total kinetic energy and ejecta velocity conditions, SN 2020znr has a higher mass ejecta than SN 2015bn. This could make probing any axisymmetry of the photosphere of the inner ejecta of SN 2020znr more difficult, on similar timescales. Which, in turn, could explain why null-polarization is still measured about 238 days after maximum light on SN 2020znr. We note on the other hand, that SN 2020znr do not seem to show any prominent post peak bumps, contrary to what has been quantified and discussed for SN 2015bn and SN 2017egm by Hosseinzadeh et al. (2021). This may also give hints why SN 2020znr does not show any sign of asymmetry at late phases.

Spectroscopy may be also informative of some differences between the 3 sources. A multi-phase spectral database of SLSNe has been tentatively classified into two classes based on spectra features analysis and template fitting procedures by Quimby et al. (2018), meaning SN 2020znr may be closer to the PTF12dam type than to the SN 2011ke type. Unfortunately, this analysis does not include spectra from neither SN 2015bn nor SN 2017egm. Another analysis on another sample of spectra of 28 type I SLSNe, including light curves retrieved from the OSC, has been investigated by Könyves-Tóth & Vinkó (2021). In their work the authors infer ejecta masses via the formalism of diffusion equations, while photospheric velocities were estimated using a method combining spectrum modelling with cross-correlation. The authors find that the W-shaped O II absorption blend, typically present in early phase spectra, is missing from the spectra of several objects having similar features to SN 2015bn. Two classes of object are therefore considered called Type W and Type 15bn. From the spectral analysis, the calculations confirm that Fast rising SLSNe generally show higher photospheric velocities close to maximum than Slow rising events. In this framework, Type 15bn events are considered as Slow evolving events, while Type W events are represented in both the Fast and Slow rising groups. Making a full analysis of the spectra of SN 2020znr is out of the scope of this work, but the comparisons of the spectra of SN 2020znr with those of PTF12dam displayed in Figure 1 infer SN 2020znr to be part of the Type W group proposed by Könyves-Tóth & Vinkó (2021). The light curve comparisons displayed in Figure 7 also infer SN 2020znr to be part of the Slow group, as does SN 2015bn. In other words, SN 2015bn and SN 2020znr could be part of two different spectral classes. On the other hand early spectra obtained on SN 2017egm clearly show that the W signature and should be a fast-rising member of the Type W group. From the sample of SLSNe discussed by Könyves-Tóth & Vinkó (2021), SN 2018hti and SN LSQ14mo are type I SLSNe members of the Type W group. Polarimetry on SN 2018hti was obtained by Lee (2019) before and after maximum light, in a total of 3 different epochs. The results are dominated by the ISP and do not show $> 3\sigma$ signal-to-noise polarization detection variations. Its light curve is similar to the one of 2015bn (Lin et al. 2020) suggesting it is part of the Slow rising event group. Polarime-

⁸ Open Supernova Catalog, <https://sne.space>

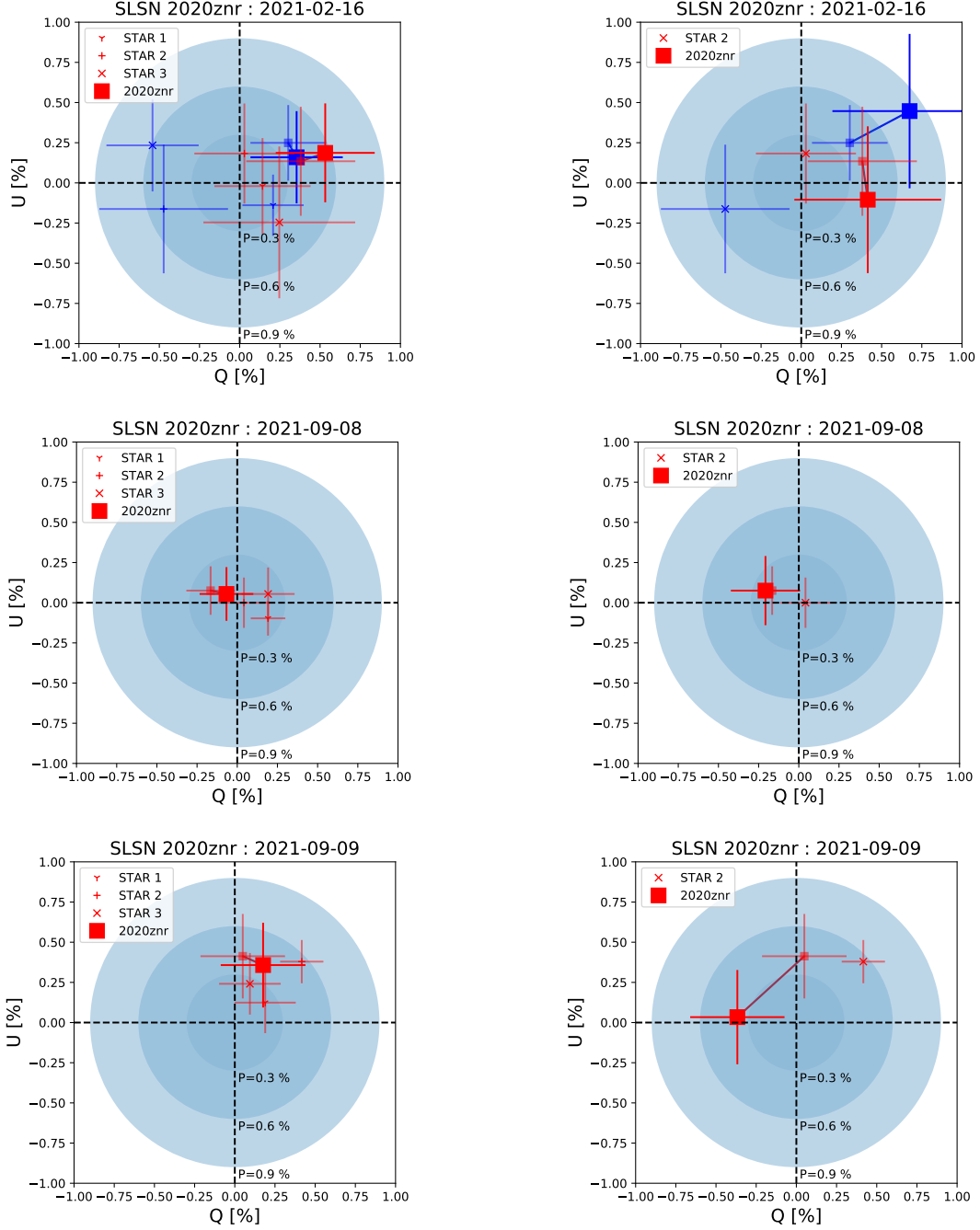


Figure 6. Left column: SN 2020znr, and field stars STAR 1, STAR 2 and STAR 3 in the $Q - U$ plane, in the plane-of-sky reference frame after instrumental polarization (IP) and zero polarization angle (ZPA) corrections (see half translucent symbols). SN 2020znr Interstellar Polarization (ISP) corrected $Q - U$ estimates have been obtained after subtraction of the IP, ZPA corrected STAR 1, STAR 2 and STAR 3, $Q - U$ weighted average estimates. The values are shown with the double sized square symbols. The double sized square symbols are connected to the half translucent square symbols to show the effect of the ISP correction in the $Q - U$ plane. Right column: same as left column when field star, STAR 2, only is used for estimating the Milky Way ISP contribution. The blue points correspond to the V filter and the red points to the R filter. Concentric discs show polarization degrees ranges up to 0.3 %, 0.6 % and 0.9 %.

Table 5. Starlight polarization from the Heiles (2000) agglomeration file catalog in the vicinity of SN 2020znr.

Star name	RA (J2000)	Dec (J2000)	GLON	GLAT	P	σ_P	θ	σ_θ	V	Heliocentric Distance	Distance to SN 2020znr
	[°]	[°]	[°]	[°]	[%]	[%]	[°]	[°]	[mag]	[pc]	[°]
HD 55052	108.109950	24.1287	193.2131	15.1134	0.02	0.035	38.2	41.2	5.7	63.1	1.67
HD 57727	110.868975	25.0506	193.3412	17.7833	0.04	0.120	45.0	56.3	5.1	50.1	1.16
HD 57702	110.852505	25.5162	192.8823	17.9453	0.04	0.069	7.3	40.8	9.0	758.6	1.22

Table 6. Possible categorization of some SLSNe that have been probed with linear polarimetry. ^(a): Könyves-Tóth & Vinkó (2021). ^(b): This work. ^(c): Nicholl et al. (2017a). ^(d): Nicholl et al. (2017b). ^(e): (Lin et al. 2020) ^(f): Inserra et al. (2016); Leloudas et al. (2017). ^(g): Saito et al. (2020). ^(h): Lee (2019). ⁽ⁱ⁾: Leloudas et al. (2015)

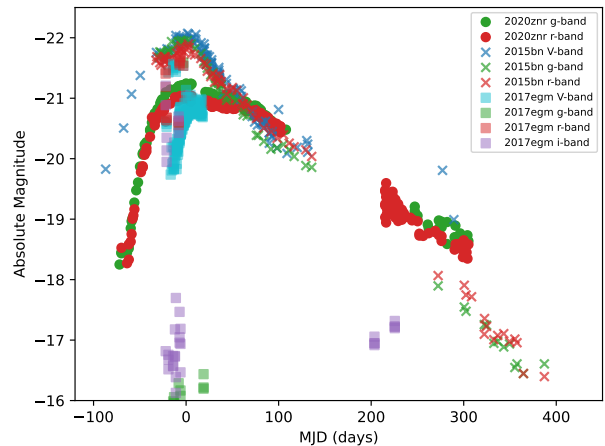
SLSN	W / 15bn ^(a) Type	Fast / Slow ^(a) rising event	P ^(b) [%]
2020znr	W ^(b)	Slow ^(b)	null ^(b)
2015bn	bn15 ^(a)	Slow ^(d)	increase with time ^(f)
2017egm	W ^(c)	Fast ^(c)	increase with time ^(g)
2018hti	W ^(a)	Slow ^(e)	null ^(h)
LSQ14mo	W ^(a)	?	null ⁽ⁱ⁾

try obtained by (Leloudas et al. 2015) on SN LSQ14mo at 5 different epochs is also found to be consistent with null-polarization detection. Unfortunately, the rising part of the light curve of SN LSQ14mo is not known, making it difficult to classify as part of the Slow or Fast rising group. All in all, these different categorization of SLSNe into several groups (W versus bn15 Type, Slow versus Fast rising event, polarized versus non-polarized system) may be useful to better understand the nature of type I SLSNe, but polarimetry data obtained at early and late epochs would be needed on a larger sample of sources for one to be able to drive any conclusions on a statistical basis. A summary of the comparisons above is given in Table 6.

Additionally, constraints on jets of SLSN-I from follow-up radio observation analysis as the ones provided by Coppejans et al. (2018) may be useful to put constraints on the geometry of the inner ejecta, and help to the interpretation of polarization measurements. It is also worth noting that imaging polarimetry and spectropolarimetry may give different polarization diagnostics if the overall electron distribution is mostly spherical, but the abundance of some element may be non-spherical. This might happen here for SN 2020znr which has been observed with broad band linear polarimetry only. SN 2015bn and SN 2017egm were both observed with linear spectropolarimetry (Inserra et al. (2016) and Saito et al. (2020) respectively), which by definition is less subject to mitigation effect of the net polarization signal due to the integration of the signal over a broader band. The increase of polarization detected on SN 2017egm was from the analysis of linear spectropolarimetry data only (Saito et al. 2020). On the other hand the increase of linear polarization observed on SN 2015bn was detected both with linear spectropolarimetry and broad band linear polarimetry ((Inserra et al. 2016).

5 SUMMARY

Optical imaging polarimetry was conducted on the hydrogen poor SLSN 2020znr during 3 phases after maximum light ($\approx +34$ days, $+288$ days and $+289$ days with respect to g-band). After instrumental

**Figure 7.** Light curves of SN 2015bn (Nicholl et al. 2016), SN 2017egm (Nicholl et al. 2017a), and SN 2020znr (this work, see section 2.2). Data from SN 2015bn and SN 2017egm were retrieved from the Open Supernova Catalog.

and interstellar polarization correction, all measurements are consistent with null-polarization detection.

The light curve including ZTF g- and r-band, and ATLAS c- and o-band data has been modelled with MOSFiT. The best fit values from the SLSN model displayed in Table 2 show that most of the characteristics of SN 2020znr are not significantly different from other SLSNe in this parameter space.

A comparison of the MOSFiT best-fit values discussed in the literature on SN 2017egm and SN 2015bn, two hydrogen poor SLSNe showing an increase of polarization after maximum light, suggests that SN 2020znr has a higher mass ejecta that may prevent access to the geometry of the inner ejecta with optical polarimetry.

The combined information provided by spectroscopy and light curve analysis may be helpful to distinguish several classes of type I SLSNe showing different polarization signatures. Such an avenue could be explored with a larger sample of SLSNe polarimetry data.

ACKNOWLEDGEMENTS

The authors would like to thank the anonymous referee for helpful comments, Matt Nicholl and Mattia Bulla for their helpful discussion, Hannu Parviainen for his kind support on the NOT, Sergio Armas Perez for providing data from the NOT public archive, and David

Young for the ATLAS python public code he developed to stack and bin ATLAS forced photometry public data.

F.P. acknowledges support from the Spanish State Research Agency (AEI) under grant number PID2019-105552RB-C43. I.P.-F. acknowledges support from the Spanish State Research Agency (AEI) under grant numbers ESP2017-86852-C4-2-R and PID2019-105552RB-C43.

Based on observations made with the Nordic Optical Telescope (NOT), owned in collaboration by the University of Turku and Aarhus University, and operated jointly by Aarhus University, the University of Turku and the University of Oslo, representing Denmark, Finland and Norway, the University of Iceland and Stockholm University at the Observatorio del Roque de los Muchachos, La Palma, Spain, of the Instituto de Astrofísica de Canarias. The data presented here were obtained in part with ALFOSC, which is provided by the Instituto de Astrofísica de Andalucía (IAA) under a joint agreement with the University of Copenhagen and NOT. Some of the data were obtained during CAT service observation Spanish time. ALFOSC polarimetry imaging data of SN 2020ank and calibration data were retrieved from the NOT public archive.

The Liverpool Telescope is operated on the island of La Palma by Liverpool John Moores University in the Spanish Observatorio del Roque de los Muchachos of the Instituto de Astrofísica de Canarias with financial support from the UK Science and Technology Facilities Council.

This work is based in part on observations obtained with the Samuel Oschin 48-inch Telescope at the Palomar Observatory as part of the Zwicky Transient Facility project. ZTF is supported by the NSF under grant AST-1440341 and a collaboration including Caltech, IPAC, the Weizmann Institute for Science, the Oskar Klein Center at Stockholm University, the University of Maryland, the University of Washington, Deutsches Elektronen-Synchrotron and Humboldt University, Los Alamos National Laboratories, the TANGO Consortium of Taiwan, the University of Wisconsin at Milwaukee, and the Lawrence Berkeley National Laboratory. Operations are conducted by the Caltech Optical Observatories (COO), the Infrared Processing and Analysis Center (IPAC), and the University of Washington (UW).

This work has made use of data from the Asteroid Terrestrial-impact Last Alert System (ATLAS) project. The Asteroid Terrestrial-impact Last Alert System (ATLAS) project is primarily funded to search for near earth asteroids through NASA grants NN12AR55G, 80NSSC18K0284, and 80NSSC18K1575; byproducts of the NEO search include images and catalogs from the survey area. This work was partially funded by Kepler/K2 grant J1944/80NSSC19K0112 and HST GO-15889, and STFC grants ST/T000198/1 and ST/S006109/1. The ATLAS science products have been made possible through the contributions of the University of Hawaii Institute for Astronomy, the Queen's University Belfast, the Space Telescope Science Institute, the South African Astronomical Observatory, and The Millennium Institute of Astrophysics (MAS), Chile.

Lasair is supported by the UKRI Science and Technology Facilities Council and is a collaboration between the University of Edinburgh (grant ST/N002512/1) and Queen's University Belfast (grant ST/N002520/1) within the LSST:UK Science Consortium.

This research has made use of “Aladin sky atlas” developed at CDS, Strasbourg Observatory, France 2000A&AS..143...33B and 2014ASPC..485..277B.

SNID is Copyright (C) 1999-2007 Stéphane Blondin and John L. Tonry, and is available under the GNU General Public License.

This work made use of the python public code

astropy/photutils: 1.0.2 release developed by Bradley et al. (2021).

This research made use of the Transient Name Server (TNS) which is the official IAU mechanism for reporting new astronomical transients such as supernova candidates, As of January 1, 2016.

This research made use of DESI LS DR9 data. The Legacy Surveys consist of three individual and complementary projects: the Dark Energy Camera Legacy Survey (DECaLS; Proposal ID #2014B-0404; PIs: David Schlegel and Arjun Dey), the Beijing-Arizona Sky Survey (BASS; NOAO Prop. ID #2015A-0801; PIs: Zhou Xu and Xiaohui Fan), and the Mayall z-band Legacy Survey (MzLS; Prop. ID #2016A-0453; PI: Arjun Dey). DECaLS, BASS and MzLS together include data obtained, respectively, at the Blanco telescope, Cerro Tololo Inter-American Observatory, NSF's NOIRLab; the Bok telescope, Steward Observatory, University of Arizona; and the Mayall telescope, Kitt Peak National Observatory, NOIRLab. The Legacy Surveys project is honored to be permitted to conduct astronomical research on Iolkam Du'ag (Kitt Peak), a mountain with particular significance to the Tohono O'odham Nation.

NOIRLab is operated by the Association of Universities for Research in Astronomy (AURA) under a cooperative agreement with the National Science Foundation.

This project used data obtained with the Dark Energy Camera (DECam), which was constructed by the Dark Energy Survey (DES) collaboration. Funding for the DES Projects has been provided by the U.S. Department of Energy, the U.S. National Science Foundation, the Ministry of Science and Education of Spain, the Science and Technology Facilities Council of the United Kingdom, the Higher Education Funding Council for England, the National Center for Supercomputing Applications at the University of Illinois at Urbana-Champaign, the Kavli Institute of Cosmological Physics at the University of Chicago, Center for Cosmology and Astro-Particle Physics at the Ohio State University, the Mitchell Institute for Fundamental Physics and Astronomy at Texas A&M University, Financiadora de Estudos e Projetos, Fundação Carlos Chagas Filho de Amparo, Financiadora de Estudos e Projetos, Fundação Carlos Chagas Filho de Amparo a Pesquisa do Estado do Rio de Janeiro, Conselho Nacional de Desenvolvimento Científico e Tecnológico and the Ministerio da Ciência, Tecnologia e Inovação, the Deutsche Forschungsgemeinschaft and the Collaborating Institutions in the Dark Energy Survey. The Collaborating Institutions are Argonne National Laboratory, the University of California at Santa Cruz, the University of Cambridge, Centro de Investigaciones Energéticas, Medioambientales y Tecnológicas-Madrid, the University of Chicago, University College London, the DES-Brazil Consortium, the University of Edinburgh, the Eidgenössische Technische Hochschule (ETH) Zurich, Fermi National Accelerator Laboratory, the University of Illinois at Urbana-Champaign, the Institut de Ciències de l'Espai (IEEC/CSIC), the Institut de Física d'Altes Energies, Lawrence Berkeley National Laboratory, the Ludwig Maximilians Universität München and the associated Excellence Cluster Universe, the University of Michigan, NSF's NOIRLab, the University of Nottingham, the Ohio State University, the University of Pennsylvania, the University of Portsmouth, SLAC National Accelerator Laboratory, Stanford University, the University of Sussex, and Texas A&M University.

The Legacy Surveys imaging of the DESI footprint is supported by the Director, Office of Science, Office of High Energy Physics of the U.S. Department of Energy under Contract No. DE-AC02-05CH1123, by the National Energy Research Scientific Computing Center, a DOE Office of Science User Facility under the same contract; and by the U.S. National Science Foundation, Division of Astronomical Sciences under Contract No. AST-0950945 to NOAO.

DATA AVAILABILITY

For science reproducibility purposes, the photometry data displayed in section B will be available online. The ESO-NTT / EFOSC2 and the LT / SPRAT spectra presented in this work are available via WISEReP.

REFERENCES

- Bailer-Jones C. A. L., Rybizki J., Fouesneau M., Demleitner M., Andrae R., 2021, *AJ*, **161**, 147
- Barkat Z., Rakavy G., Sack N., 1967, *Phys. Rev. Lett.*, **18**, 379
- Bellm E. C., et al., 2019, *PASP*, **131**, 018002
- Blanchard P. K., Berger E., Nicholl M., Villar V. A., 2020, *ApJ*, **897**, 114
- Blondin S., Tonry J. L., 2007, *ApJ*, **666**, 1024
- Bradley L., et al., 2021, *astropy/photutils: 1.0.2*, doi:10.5281/zenodo.4453725
- Brown P. J., et al., 2016, *ApJ*, **828**, 3
- Chen T. W., et al., 2021, arXiv e-prints, p. arXiv:2109.07942
- Cikota A., et al., 2018, *MNRAS*, **479**, 4984
- Coppejans D. L., et al., 2018, *ApJ*, **856**, 56
- Coppejans D. L., et al., 2021a, *The Astronomer's Telegram*, **14393**, 1
- Coppejans D. L., et al., 2021b, *The Astronomer's Telegram*, **14418**, 1
- De Cia A., et al., 2018, *ApJ*, **860**, 100
- Dessart L., Hillier D. J., Waldman R., Livne E., Blondin S., 2012, *MNRAS*, **426**, L76
- Eftekhari T., et al., 2019, *ApJ*, **876**, L10
- Eftekhari T., et al., 2021, *ApJ*, **912**, 21
- Fraley G. S., 1968, *Ap&SS*, **2**, 96
- Gal-Yam A., 2019a, *ARA&A*, **57**, 305
- Gal-Yam A., 2019b, *ApJ*, **882**, 102
- Ginzburg S., Balberg S., 2012, *ApJ*, **757**, 178
- Gomez S., Berger E., Blanchard P. K., Hosseinzadeh G., Nicholl M., Villar V. A., Yin Y., 2020, *ApJ*, **904**, 74
- Guillochon J., Parrent J., Kelley L. Z., Margutti R., 2017, *ApJ*, **835**, 64
- Guillochon J., Nicholl M., Villar V. A., Mockler B., Narayan G., Mandel K. S., Berger E., Williams P. K. G., 2018, *ApJS*, **236**, 6
- Hatsukade B., Tominaga N., Morokuma T., Morokuma-Matsui K., Matsuda Y., Tamura Y., Niinuma K., Motogi K., 2021a, arXiv e-prints, p. arXiv:2108.10445
- Hatsukade B., et al., 2021b, *ApJ*, **911**, L1
- Heiles C., 2000, *AJ*, **119**, 923
- Higson E., Handley W., Hobson M., Lasenby A., 2019, *Statistics and Computing*, **29**, 891
- Hosseinzadeh G., Berger E., Metzger B. D., Gomez S., Nicholl M., Blanchard P., 2021, arXiv e-prints, p. arXiv:2109.09743
- Ihanc N., Gromadzki M., Wevers T., Irani I., 2020, *Transient Name Server Classification Report*, **2020-3486**, 1
- Inserra C., Bulla M., Sim S. A., Smartt S. J., 2016, *ApJ*, **831**, 79
- Inserra C., et al., 2017, *MNRAS*, **468**, 4642
- Jerkstrand A., Smartt S. J., Heger A., 2016, *MNRAS*, **455**, 3207
- Jerkstrand A., et al., 2017, *ApJ*, **835**, 13
- Kasen D., Bildsten L., 2010, *ApJ*, **717**, 245
- Kashiyama K., Murase K., Bartos I., Kiuchi K., Margutti R., 2016, *ApJ*, **818**, 94
- Könyves-Tóth R., Vinkó J., 2021, *ApJ*, **909**, 24
- Kozyreva A., Kromer M., Noebauer U. M., Hirschi R., 2018, *MNRAS*, **479**, 3106
- Kumar A., et al., 2021, *MNRAS*, **502**, 1678
- Law C. J., et al., 2019, *ApJ*, **886**, 24
- Lee C.-H., 2019, *ApJ*, **875**, 121
- Lee C.-H., 2020, *Astronomische Nachrichten*, **341**, 651
- Leloudas G., et al., 2015, *ApJ*, **815**, L10
- Leloudas G., et al., 2017, *ApJ*, **837**, L14
- Levan A. J., Read A. M., Metzger B. D., Wheatley P. J., Tanvir N. R., 2013, *ApJ*, **771**, 136
- Lin W. L., et al., 2020, *MNRAS*, **497**, 318
- Lobo Gomes A., Magalhães A. M., Pereyra A., Rodrigues C. V., 2015, *ApJ*, **806**, 94
- Lunnan R., et al., 2016, *ApJ*, **831**, 144
- Lunnan R., et al., 2018a, *Nature Astronomy*, **2**, 887
- Lunnan R., et al., 2018b, *ApJ*, **852**, 81
- Lunnan R., et al., 2020, *ApJ*, **901**, 61
- Magalhaes A. M., Benedetti E., Roland E. H., 1984, *PASP*, **96**, 383
- Margutti R., et al., 2018, *ApJ*, **864**, 45
- Maund J. R., Steele I., Jermak H., Wheeler J. C., Wiersema K., 2019, *MNRAS*, **482**, 4057
- Maund J. R., Leloudas G., Malesani D. B., Patat F., Sollerman J., de Ugarte Postigo A., 2020, *MNRAS*, **498**, 3730
- Maund J. R., et al., 2021, *MNRAS*, **503**, 312
- Metzger B. D., Vurm I., Hascoët R., Beloborodov A. M., 2014, *MNRAS*, **437**, 703
- Milislavljevic D., Patnaude D. J., Chevalier R. A., Raymond J. C., Fesen R. A., Margutti R., Conner B., Banovetz J., 2018, *ApJ*, **864**, L36
- Mondal S., Bera A., Chandra P., Das B., 2020, *MNRAS*, **498**, 3863
- Moriya T. J., Sorokina E. I., Chevalier R. A., 2018, *Space Sci. Rev.*, **214**, 59
- Murase K., Kashiyama K., Kiuchi K., Bartos I., 2015, *ApJ*, **805**, 82
- Murase K., et al., 2021, *MNRAS*,
- Naghizadeh-Khouei J., Clarke D., 1993, *A&A*, **274**, 968
- Nicholl M., 2021a, arXiv e-prints, p. arXiv:2109.08697
- Nicholl M., 2021b, arXiv e-prints, p. arXiv:2109.08697
- Nicholl M., et al., 2014, *MNRAS*, **444**, 2096
- Nicholl M., et al., 2016, *ApJ*, **826**, 39
- Nicholl M., Berger E., Margutti R., Blanchard P. K., Guillochon J., Leja J., Chornock R., 2017a, *ApJ*, **845**, L8
- Nicholl M., Guillochon J., Berger E., 2017b, *ApJ*, **850**, 55
- Nordin J., Brinnel V., Giomi M., Santen J. V., Gal-Yam A., Yaron O., Schulze S., 2020, *Transient Name Server Discovery Report*, **2020-3443**, 1
- Omand C. M. B., Kashiyama K., Murase K., 2018, *MNRAS*, **474**, 573
- Omand C. M. B., Kashiyama K., Murase K., 2019, *MNRAS*, **484**, 5468
- Ostriker J. P., Gunn J. E., 1971, *ApJ*, **164**, L95
- Pastorello A., et al., 2010, *ApJ*, **724**, L16
- Perley D. A., et al., 2016, *ApJ*, **830**, 13
- Piascik A. S., Steele I. A., Bates S. D., Mottram C. J., Smith R. J., Barnsley R. M., Bolton B., 2014, in Ramsay S. K., McLean I. S., Takami H., eds, *Society of Photo-Optical Instrumentation Engineers (SPIE) Conference Series Vol. 9147, Ground-based and Airborne Instrumentation for Astronomy V*. p. 91478H, doi:10.1117/12.2055117
- Planck Collaboration et al., 2020, *A&A*, **641**, A1
- Quimby R. M., et al., 2011, *Nature*, **474**, 487
- Quimby R. M., et al., 2018, *ApJ*, **855**, 2
- Rakavy G., Shaviv G., 1967, *ApJ*, **148**, 803
- Ramírez E. A., Magalhães A. M., Davidson James W. J., Pereyra A., Rubinho M., 2017, *PASP*, **129**, 055001
- Saito S., et al., 2020, *ApJ*, **894**, 154
- Sánchez-Sáez P., et al., 2021, *AJ*, **161**, 141
- Schulze S., et al., 2018, *MNRAS*, **473**, 1258
- Schulze S., et al., 2021, *ApJS*, **255**, 29
- Smartt S. J., et al., 2017, *Nature*, **551**, 75
- Smith N., 2014, *ARA&A*, **52**, 487
- Smith N., Chornock R., Silverman J. M., Filippenko A. V., Foley R. J., 2010, *ApJ*, **709**, 856
- Smith K. W., et al., 2019, *Research Notes of the American Astronomical Society*, **3**, 26
- Speagle J. S., 2020, *MNRAS*, **493**, 3132
- Steele I. A., et al., 2004, in Oschmann Jacobus M. J., ed., *Society of Photo-Optical Instrumentation Engineers (SPIE) Conference Series Vol. 5489, Ground-based Telescopes*. pp 679–692, doi:10.1117/12.551456
- Tolstov A., Nomoto K., Blinnikov S., Sorokina E., Quimby R., Baklanov P., 2017, *ApJ*, **835**, 266
- Tonry J. L., et al., 2018, *PASP*, **130**, 064505
- Tran H. D., 1995, *ApJ*, **440**, 565
- Turnshek D. A., Bohlin R. C., Williamson R. L. I., Lupie O. L., Koornneef J., Morgan D. H., 1990, *AJ*, **99**, 1243
- Villar V. A., Nicholl M., Berger E., 2018, *ApJ*, **869**, 166

Table A1. Polarimetry results obtained in this work and by Lee (2020) after data reduction of the ALFOSC data obtained on March 1, 2020 on SN 2020ank. ^(a): Highly polarized standard star. ^(b): unpolarized standard star.

Object	P [%]	
	Lee (2020)	This work
2020ank	0.6 ± 0.3	0.5 ± 0.2
HD236928 ^(a)	6.8 ± 0.1	6.7 ± 0.1
HD64299 ^(b)	0.1 ± 0.1	0.1 ± 0.1

Woosley S. E., 2010, *ApJ*, 719, L204

Woosley S. E., 2017, *ApJ*, 836, 244

Yan L., et al., 2017, *ApJ*, 848, 6

Yin Y., Gomez S., Berger E., Hosseinzadeh G., Nicholl M., Blanchard P. K., 2021, arXiv e-prints, p. arXiv:2109.06970

APPENDIX A: TEST ON OUR POLARIZATION DATA REDUCTION PIPELINE

We ran our polarimetry data reduction pipeline on the ALFOSC archival data obtained on SN 2020ank by Lee (2020). Our results are displayed in Table A1 for comparison. Note that polarized star HD251204 reported in Table 2 from Lee (2020) is actually polarized star HD236928, as from the coordinates displayed in the fits header of the ALFOSC dataframes. The outputs obtained with the two methods are consistent with each other within the uncertainties.

APPENDIX B: PHOTOMETRY TABLE

The photometry from SN 2020znr used along this work is compiled in Table B1, Table B2, Table B3, Table B4, Table B5 and Table B6.

This paper has been typeset from a $\text{\TeX}/\text{\LaTeX}$ file prepared by the author.

Table B1. ZTF and ATLAS photometry.

MJD	Magnitude	$\sigma_{\text{Magnitude}}$	band	survey
59145.600000	22.620	3.554	o	ATLAS
59147.580000	21.677	1.532	c	ATLAS
59153.560000	21.827	3.241	o	ATLAS
59155.411944	20.034	0.314	g	ZTF
59157.399086	19.848	0.328	g	ZTF
59157.399549	19.832	0.352	g	ZTF
59157.479387	19.758	0.282	r	ZTF
59163.440486	19.840	0.150	g	ZTF
59163.503276	20.012	0.152	r	ZTF
59163.560000	20.312	0.482	o	ATLAS
59165.393819	19.768	0.118	g	ZTF
59165.421620	19.702	0.127	r	ZTF
59165.422083	19.953	0.151	r	ZTF
59165.444097	19.710	0.113	g	ZTF
59167.470729	19.656	0.132	r	ZTF
59167.506516	19.434	0.116	g	ZTF
59168.436412	19.531	0.112	r	ZTF
59168.478322	19.317	0.087	g	ZTF
59169.468345	19.265	0.089	g	ZTF
59169.505590	19.277	0.123	r	ZTF
59170.404248	19.222	0.086	r	ZTF
59171.416829	19.009	0.068	g	ZTF
59171.477951	19.121	0.096	r	ZTF
59173.443137	18.807	0.096	g	ZTF
59175.421458	18.676	0.199	g	ZTF
59175.620000	18.682	0.112	c	ATLAS
59177.516759	18.413	0.063	g	ZTF
59178.540741	18.506	0.066	r	ZTF
59179.520000	18.558	0.114	o	ATLAS
59180.451736	18.409	0.079	r	ZTF
59180.496250	18.215	0.079	g	ZTF
59180.496724	18.193	0.067	g	ZTF
59180.539271	18.427	0.138	r	ZTF
59181.340000	18.419	0.319	o	ATLAS
59182.463900	18.200	0.072	r	ZTF
59182.464363	18.220	0.058	r	ZTF
59182.529329	18.147	0.082	g	ZTF
59182.529792	18.050	0.080	g	ZTF
59183.420000	18.070	0.172	o	ATLAS
59184.429444	18.032	0.063	g	ZTF
59184.436053	18.012	0.071	g	ZTF
59184.464363	18.163	0.069	r	ZTF
59184.480845	18.108	0.077	r	ZTF
59188.368275	17.922	0.059	r	ZTF
59188.445347	17.803	0.053	g	ZTF
59188.445810	17.819	0.053	g	ZTF
59189.470000	17.997	0.094	o	ATLAS
59190.370405	17.685	0.047	g	ZTF
59190.436458	17.601	0.231	r	ZTF
59191.460000	17.824	0.058	o	ATLAS
59192.480000	17.627	0.043	c	ATLAS
59193.308009	17.684	0.052	r	ZTF
59193.357211	17.545	0.037	g	ZTF
59193.434907	17.532	0.033	g	ZTF
59193.499178	17.733	0.061	r	ZTF
59193.550000	17.756	0.044	o	ATLAS
59195.479213	17.629	0.048	r	ZTF
59195.560000	17.522	0.036	c	ATLAS
59196.394317	17.582	0.038	r	ZTF
59196.423449	17.462	0.053	g	ZTF
59197.410000	17.461	0.035	c	ATLAS
59198.429722	17.593	0.043	r	ZTF

Table B2. ZTF and ATLAS photometry.

MJD	Magnitude	$\sigma_{\text{Magnitude}}$	band	survey
59199.299664	17.516	0.050	r	ZTF
59199.424861	17.364	0.028	g	ZTF
59200.342558	17.536	0.081	r	ZTF
59200.432095	17.331	0.050	g	ZTF
59201.412697	17.302	0.029	g	ZTF
59201.458252	17.464	0.037	r	ZTF
59203.313333	17.304	0.031	g	ZTF
59203.344803	17.294	0.038	g	ZTF
59203.431690	17.486	0.051	r	ZTF
59203.433588	17.421	0.037	r	ZTF
59205.215961	17.394	0.041	r	ZTF
59205.301782	17.186	0.032	g	ZTF
59205.319757	17.670	0.050	r	ZTF
59205.380776	17.209	0.050	g	ZTF
59205.520000	17.299	0.029	c	ATLAS
59207.430000	17.400	0.052	o	ATLAS
59209.420000	17.380	0.056	o	ATLAS
59210.263762	17.140	0.043	g	ZTF
59210.387604	17.374	0.043	r	ZTF
59215.297755	17.268	0.075	r	ZTF
59215.337269	17.151	0.064	g	ZTF
59216.316215	17.318	0.041	r	ZTF
59216.423947	17.125	0.059	g	ZTF
59217.325949	17.287	0.037	r	ZTF
59217.520000	17.398	0.050	o	ATLAS
59218.265845	17.116	0.042	g	ZTF
59218.402974	17.330	0.042	r	ZTF
59219.279317	17.084	0.027	g	ZTF
59219.302188	17.269	0.037	r	ZTF
59219.490000	17.350	0.047	o	ATLAS
59220.297824	17.303	0.040	r	ZTF
59220.339352	17.093	0.044	g	ZTF
59221.234606	17.246	0.040	r	ZTF
59221.318472	17.075	0.033	g	ZTF
59221.410000	17.171	0.027	c	ATLAS
59222.338796	17.302	0.052	r	ZTF
59222.382951	17.095	0.034	g	ZTF
59223.296285	17.257	0.039	r	ZTF
59223.351829	17.067	0.034	g	ZTF
59223.480000	17.202	0.070	c	ATLAS
59224.288681	17.278	0.036	r	ZTF
59225.238461	17.078	0.039	g	ZTF
59226.387257	17.075	0.040	g	ZTF
59227.297222	17.233	0.040	r	ZTF
59227.342107	17.040	0.038	g	ZTF
59227.600000	17.148	0.031	c	ATLAS
59228.265185	17.090	0.037	g	ZTF
59228.318634	17.302	0.039	r	ZTF
59229.221076	17.100	0.041	g	ZTF
59229.333032	17.259	0.038	r	ZTF
59229.470000	17.144	0.031	c	ATLAS
59230.244039	17.257	0.042	r	ZTF
59230.328750	17.075	0.051	g	ZTF
59231.234178	17.081	0.031	g	ZTF
59231.311794	17.251	0.038	r	ZTF
59231.360000	17.127	0.029	c	ATLAS
59232.372373	17.339	0.058	r	ZTF
59232.394526	17.042	0.040	g	ZTF
59233.277859	17.243	0.044	r	ZTF
59233.323391	17.049	0.027	g	ZTF
59235.430000	17.350	0.071	o	ATLAS
59245.430000	17.398	0.051	o	ATLAS

Table B3. ZTF and ATLAS photometry.

MJD	Magnitude	$\sigma_{\text{Magnitude}}$	band	survey
59248.228542	17.181	0.042	g	ZTF
59248.236898	17.367	0.037	r	ZTF
59249.219618	17.208	0.071	g	ZTF
59249.310660	17.325	0.039	r	ZTF
59250.256655	17.222	0.040	g	ZTF
59250.328484	17.389	0.046	r	ZTF
59251.216262	17.326	0.034	r	ZTF
59251.275498	17.185	0.028	g	ZTF
59251.410000	17.265	0.035	c	ATLAS
59252.204317	17.397	0.045	r	ZTF
59252.287187	17.213	0.036	g	ZTF
59253.199132	17.199	0.035	g	ZTF
59253.297789	17.357	0.044	r	ZTF
59253.360000	17.268	0.032	c	ATLAS
59254.202639	17.415	0.050	r	ZTF
59254.227951	17.206	0.039	g	ZTF
59255.186354	17.232	0.028	g	ZTF
59255.297766	17.427	0.074	r	ZTF
59255.390000	17.303	0.034	c	ATLAS
59256.213113	17.426	0.052	r	ZTF
59256.296319	17.211	0.050	g	ZTF
59257.214421	17.363	0.038	r	ZTF
59257.390000	17.252	0.033	c	ATLAS
59260.192523	17.262	0.047	g	ZTF
59260.249977	17.410	0.039	r	ZTF
59261.340000	17.245	0.030	c	ATLAS
59262.191921	17.396	0.043	r	ZTF
59262.276562	17.260	0.028	g	ZTF
59263.213750	17.420	0.051	r	ZTF
59263.277813	17.260	0.049	g	ZTF
59264.191111	17.389	0.039	r	ZTF
59264.282326	17.266	0.038	g	ZTF
59265.187778	17.298	0.042	g	ZTF
59265.212002	17.427	0.043	r	ZTF
59265.330000	17.594	0.961	o	ATLAS
59266.133750	17.260	0.055	g	ZTF
59266.212928	17.376	0.041	r	ZTF
59267.174965	17.450	0.042	r	ZTF
59267.253657	17.283	0.051	g	ZTF
59270.233553	17.273	0.052	g	ZTF
59270.295313	17.398	0.066	r	ZTF
59271.225451	17.225	0.036	g	ZTF
59271.258333	17.460	0.053	r	ZTF
59272.170428	17.279	0.048	g	ZTF
59272.214144	17.365	0.047	r	ZTF
59273.173437	17.249	0.048	g	ZTF
59273.212153	17.436	0.050	r	ZTF
59274.166250	17.325	0.054	g	ZTF
59274.256100	17.396	0.067	r	ZTF
59275.172106	17.277	0.041	g	ZTF
59276.211238	17.294	0.025	g	ZTF
59276.282407	17.382	0.049	r	ZTF
59277.340000	17.322	0.029	c	ATLAS
59278.185938	17.461	0.046	r	ZTF
59280.150150	17.395	0.045	r	ZTF
59280.150150	17.395	0.045	r	ZTF
59280.152998	17.457	0.047	r	ZTF
59280.152998	17.457	0.047	r	ZTF
59280.210995	17.298	0.049	g	ZTF
59280.210995	17.298	0.049	g	ZTF
59280.211470	17.273	0.027	g	ZTF
59280.211470	17.273	0.027	g	ZTF

Table B4. ZTF and ATLAS photometry.

MJD	Magnitude	$\sigma_{\text{Magnitude}}$	band	survey
59287.300000	17.349	0.042	c	ATLAS
59290.213958	17.383	0.048	g	ZTF
59290.214421	17.336	0.036	g	ZTF
59290.239167	17.465	0.043	r	ZTF
59290.239630	17.429	0.041	r	ZTF
59291.360000	17.385	0.040	c	ATLAS
59292.173160	17.366	0.044	g	ZTF
59292.174120	17.344	0.044	g	ZTF
59292.196875	17.460	0.041	r	ZTF
59292.214398	17.499	0.054	r	ZTF
59293.310000	17.518	0.041	o	ATLAS
59294.170185	17.385	0.040	g	ZTF
59294.208137	17.496	0.047	r	ZTF
59299.350000	17.794	1.354	o	ATLAS
59301.177975	17.573	0.048	r	ZTF
59301.178449	17.483	0.034	r	ZTF
59301.215012	17.404	0.051	g	ZTF
59301.234606	17.442	0.048	g	ZTF
59303.156852	17.487	0.040	r	ZTF
59303.196296	17.423	0.047	g	ZTF
59303.218426	17.410	0.046	g	ZTF
59303.242743	17.565	0.052	r	ZTF
59305.350000	17.537	0.055	o	ATLAS
59306.157986	17.451	0.037	g	ZTF
59306.181944	17.477	0.042	g	ZTF
59306.195255	17.545	0.043	r	ZTF
59306.226482	17.584	0.047	r	ZTF
59308.159514	17.479	0.036	g	ZTF
59308.186435	17.529	0.057	r	ZTF
59308.186910	17.603	0.047	r	ZTF
59308.247130	17.494	0.042	g	ZTF
59310.184317	17.617	0.046	r	ZTF
59310.184780	17.579	0.045	r	ZTF
59312.172523	17.632	0.043	r	ZTF
59312.172986	17.575	0.038	r	ZTF
59312.206262	17.579	0.045	g	ZTF
59312.206736	17.558	0.048	g	ZTF
59313.290000	17.588	0.039	c	ATLAS
59314.184826	17.639	0.049	r	ZTF
59314.205949	17.577	0.048	g	ZTF
59314.206424	17.614	0.046	g	ZTF
59316.160012	17.683	0.048	r	ZTF
59316.160475	17.607	0.053	r	ZTF
59316.207026	17.631	0.043	g	ZTF
59316.207500	17.632	0.051	g	ZTF
59319.174988	17.652	0.053	g	ZTF
59319.175463	17.684	0.033	g	ZTF
59319.270000	17.710	0.057	o	ATLAS
59321.163808	17.688	0.054	g	ZTF
59321.174248	17.697	0.056	g	ZTF
59321.200521	17.763	0.052	r	ZTF
59321.220972	17.681	0.054	r	ZTF
59321.250000	17.778	0.058	o	ATLAS
59325.185799	17.706	0.052	r	ZTF
59325.186262	17.809	0.071	r	ZTF
59325.199213	17.730	0.049	g	ZTF
59325.199676	17.774	0.059	g	ZTF
59327.240000	17.815	0.108	o	ATLAS
59329.166956	17.779	0.055	g	ZTF
59329.166956	17.779	0.055	g	ZTF
59329.198681	17.845	0.070	r	ZTF
59329.198681	17.845	0.070	r	ZTF

Table B5. ZTF and ATLAS photometry.

MJD	Magnitude	$\sigma_{\text{Magnitude}}$	band	survey
59329.199630	17.749	0.062	r	ZTF
59329.199630	17.749	0.062	r	ZTF
59329.280000	17.755	0.111	o	ATLAS
59331.290000	17.892	0.267	o	ATLAS
59335.217083	17.803	0.073	g	ZTF
59337.270000	17.905	0.062	o	ATLAS
59345.260000	17.912	0.085	o	ATLAS
59347.260000	17.937	0.081	c	ATLAS
59442.499815	19.253	0.232	r	ZTF
59442.502199	19.035	0.197	r	ZTF
59442.504595	18.824	0.188	r	ZTF
59442.506991	19.059	0.262	r	ZTF
59442.509387	18.803	0.233	r	ZTF
59443.498819	19.339	0.281	r	ZTF
59443.501215	19.247	0.299	r	ZTF
59443.503611	18.916	0.273	r	ZTF
59443.508403	18.688	0.239	r	ZTF
59444.499178	19.190	0.215	r	ZTF
59444.501574	19.076	0.221	r	ZTF
59444.503970	19.116	0.235	r	ZTF
59446.502002	19.071	0.174	r	ZTF
59446.504363	19.147	0.183	r	ZTF
59446.506725	19.151	0.214	r	ZTF
59446.509097	19.143	0.268	r	ZTF
59449.506644	18.839	0.293	r	ZTF
59449.509051	18.888	0.282	r	ZTF
59450.493831	18.896	0.241	r	ZTF
59450.498669	18.966	0.268	r	ZTF
59450.501099	18.830	0.217	r	ZTF
59450.505914	18.952	0.326	r	ZTF
59450.508310	18.935	0.241	r	ZTF
59450.513113	18.973	0.316	r	ZTF
59451.490984	19.053	0.172	r	ZTF
59451.510382	19.081	0.187	r	ZTF
59451.512778	19.191	0.177	r	ZTF
59452.494919	19.045	0.167	r	ZTF
59452.499861	19.115	0.191	r	ZTF
59452.502338	19.108	0.118	r	ZTF
59453.491319	18.959	0.111	r	ZTF
59453.493796	19.248	0.166	r	ZTF
59453.496262	19.144	0.124	r	ZTF
59453.498727	19.256	0.138	r	ZTF
59453.501192	19.163	0.157	r	ZTF
59454.493171	19.099	0.141	r	ZTF
59454.495648	19.178	0.172	r	ZTF
59454.498113	19.203	0.144	r	ZTF
59454.503067	19.155	0.148	r	ZTF
59455.620000	18.987	0.344	o	ATLAS
59456.495729	19.142	0.154	r	ZTF
59456.498241	19.033	0.124	r	ZTF
59456.500764	19.314	0.155	r	ZTF
59456.505810	19.057	0.130	r	ZTF
59460.495660	19.275	0.123	r	ZTF
59460.498194	19.293	0.115	r	ZTF
59460.500729	19.127	0.105	r	ZTF
59460.503264	19.168	0.114	r	ZTF
59460.505799	19.241	0.120	r	ZTF
59461.494711	19.263	0.112	r	ZTF
59461.497245	19.245	0.115	r	ZTF
59461.499780	19.248	0.112	r	ZTF
59461.502315	19.260	0.126	r	ZTF
59461.504850	19.201	0.089	r	ZTF

Table B6. ZTF and ATLAS photometry.

MJD	Magnitude	$\sigma_{\text{Magnitude}}$	band	survey
59462.496401	19.191	0.112	r	ZTF
59462.498924	19.183	0.093	r	ZTF
59462.501435	19.243	0.128	r	ZTF
59462.503947	19.248	0.109	r	ZTF
59462.506470	19.257	0.122	r	ZTF
59467.580000	19.076	0.226	c	ATLAS
59469.475440	19.258	0.113	r	ZTF
59469.620000	19.160	0.330	o	ATLAS
59471.471319	19.304	0.159	r	ZTF
59472.451921	19.263	0.141	g	ZTF
59472.495880	19.296	0.118	r	ZTF
59474.449583	19.152	0.151	g	ZTF
59474.450058	19.076	0.113	g	ZTF
59477.468634	19.226	0.175	g	ZTF
59477.469109	19.297	0.169	g	ZTF
59477.494433	19.318	0.131	r	ZTF
59479.446412	19.556	0.239	r	ZTF
59479.447824	19.524	0.257	r	ZTF
59479.590000	19.112	0.395	o	ATLAS
59483.487095	19.561	0.174	r	ZTF
59485.570000	19.295	0.468	o	ATLAS
59488.498125	19.373	0.125	g	ZTF
59489.476007	19.516	0.145	r	ZTF
59489.487616	19.432	0.109	g	ZTF
59491.620000	19.368	0.299	o	ATLAS
59493.580000	19.596	0.439	o	ATLAS
59496.455255	19.498	0.133	r	ZTF
59496.463044	19.480	0.126	r	ZTF
59496.487535	19.484	0.168	g	ZTF
59500.444896	19.434	0.163	g	ZTF
59500.445370	19.305	0.116	g	ZTF
59500.487569	19.549	0.126	r	ZTF
59501.570000	19.642	0.390	o	ATLAS
59503.374618	19.645	0.232	r	ZTF
59503.423819	19.566	0.187	r	ZTF
59503.479329	19.326	0.094	g	ZTF
59503.497211	19.417	0.134	g	ZTF
59505.590000	19.691	0.564	o	ATLAS
59507.590000	19.485	0.470	o	ATLAS
59509.422280	19.331	0.170	g	ZTF
59509.422743	19.695	0.217	g	ZTF
59509.510000	19.631	0.870	o	ATLAS
59511.530000	19.227	3.074	o	ATLAS
59515.610000	19.396	0.820	o	ATLAS
59517.465984	19.582	0.109	g	ZTF
59517.503484	19.788	0.147	r	ZTF
59517.580000	20.063	0.511	o	ATLAS
59518.373831	19.391	0.090	g	ZTF
59518.491493	19.698	0.111	r	ZTF
59519.570000	19.999	0.411	o	ATLAS
59521.451019	19.695	0.108	r	ZTF
59521.500000	19.759	0.488	o	ATLAS
59522.456447	19.590	0.115	g	ZTF
59523.449456	19.519	0.091	g	ZTF
59523.499363	19.738	0.132	r	ZTF
59523.570000	19.479	0.262	c	ATLAS
59524.446979	19.733	0.123	r	ZTF
59524.508090	19.575	0.115	g	ZTF
59525.455880	19.787	0.105	r	ZTF
59525.466505	19.628	0.110	g	ZTF
59525.500000	19.574	0.360	o	ATLAS
59526.448993	19.576	0.094	g	ZTF

Table B7. ZTF and ATLAS photometry.

MJD	Magnitude	$\sigma_{\text{Magnitude}}$	band	survey
59526.488171	19.911	0.162	r	ZTF
59527.373715	19.633	0.266	r	ZTF
59527.520000	19.704	0.293	c	ATLAS
59529.382893	19.640	0.142	g	ZTF
59529.406782	19.909	0.148	r	ZTF
59529.530000	20.207	0.510	o	ATLAS
59530.406505	19.607	0.209	g	ZTF
59530.443368	19.832	0.242	r	ZTF
59531.380162	19.550	0.121	g	ZTF
59531.421238	19.936	0.132	r	ZTF
59532.416273	19.646	0.115	g	ZTF
59532.436007	19.702	0.163	r	ZTF